RESEARCH

Numerical Study of Metal Nano-Orifices for Optical Sizing of Ultrafine Particles in Aerosols

Sophia Judge[1] · Juan Jaramillo[1] · Hao Jiang[1] ⬤

Abstract

Optical particle sizers are widely used aerosol instruments which detect pulses of light scattered from individual airborne particles to measure their sizes. Existing optical particle sizers based on conventional optics generally cannot measure particles with diameters smaller than 100 nm, known as ultrafine particles, because optical signals are too weak due to dominant Rayleigh scattering in this particle size range. To address this challenge, we propose to harvest the nanoscale light confinement effects from nanostructures to boost the optical signals for sizing ultrafine particles. In this work, we numerically studied a nano-optical particle sizer based on a metal nano-orifice, essentially a subwavelength nano-aperture in a metal thin film with a flow-through nanofluidic channel for aerosols. When an ultrafine particle travels through the metal nano-orifice, the light transmission through the orifice gives a pulsatile optical signal, and its pulse height is correlated with the particle size. We modeled the optical responses of the metal nano-orifice using finite difference time domain simulation and the aerodynamic behaviors of ultrafine particles using finite element analysis and particle tracing technique. The numerical results suggest that ultrafine particles can be effectively sized through the metal nano-orifice. The pulse heights are found to be proportional to the third power of particle diameter and remain consistent when particle trajectories inside the orifice vary widely. This work is the first theoretical investigation of plasmonic sensors for aerosol particles. The ability of the metal nano-orifice to size ultrafine particles lays the foundation for further breakthroughs in optical-based aerosol sensing techniques.

Introduction

Ultrafine particles (UFPs) or $PM_{0.1}$ refer to airborne particles with aerodynamic diameters smaller than 100 nm. Ultrafine particles can be generated from many different sources including wildfire smoke, combustion of fossil fuels, airborne viruses, and cigarette smoke. These particles can potentially pose severe health risks as they can enter the human body through the lungs and be transported to essentially all organs [1, 2]. Long-term exposure to ultrafine particles was found to be associated with an increased risk of cardiovascular disease, myocardial infarction, and heart failure [3]. To understand the mechanisms of how ultrafine particles affect the human body, fundamental physical and chemical characteristics must be reliably measured. One such key parameter is the particle size distribution, i.e., the particle concentrations as a function of particle diameter.

An optical particle sizer (OPS) implements a laser beam and a photodetector to measure light scattered from individual particles in an aerosol. The particle sizes are calculated from the heights of optical pulses induced by individual airborne particles. An optical particle sizer is usually used as a non-intrusive approach to size airborne particles with diameters comparable with laser wavelength. Mie scattering is dominant in this size range, which gives relatively strong optical signals [4]. Optical particle sizers based on conventional optics usually have a sizing limit (i.e., smallest detectable particle size) of about 300 nm. As the particle

✉ Hao Jiang
hjiang@ltu.edu

Sophia Judge
sjudge@ltu.edu

Juan Jaramillo
jaramillo.jd@outlook.com

1 Department of Biomedical Engineering, Lawrence Technological University, 21000 W 10 Mile Rd, Southfield 48075, MI, USA

size scales down beyond this range, the intensity of scattered light decreases sharply, which poses severe challenges for optical systems to distinguish optical pulses from noise. For ultrafine particles which have diameters smaller than 100 nm, Rayleigh scattering becomes the primary effect, and the scattered light intensity has a 6th power dependence on particle diameter [4]. Due to the very weak optical signals, an optical particle sizer is generally not a practical option for measuring ultrafine particles. Certain optical particle sizers with advanced optics and electronics design can extend the sizing limit into about the 90 nm range, but still can only cover the range of ultrafine particles marginally [5–8].

Existing reliable approaches for sizing ultrafine particles, such as scanning mobility particle sizer (SMPS), fast mobility particle sizer (FMPS), and condensation particle counter (CPC), are all intrusive by nature. Both SMPS and FMPS have to deposit electrical charges onto ultrafine particles, and a CPC must grow ultrafine particles into much larger particles to become optically detectable. These intrusive measurements are acceptable for most types of particles, but can fundamentally disrupt the structures of biological particles, such as virus particles [9]. It would be ideal if biological ultrafine particles can be sized using non-intrusive approaches, such as OPS-based techniques.

Metal nano-apertures refer to subwavelength nano-apertures in metal films with aperture dimensions smaller than the wavelength of incident light. Metal nano-apertures can confine light into nanoscale dimensions [10–13], which can enable intriguing applications including biosensing [14, 15], optical trapping [16–21], surface-enhanced Raman scattering (SERS) [22, 23], and enhancement of light emitters [24, 25]. Optical transmission through a single metal nano-aperture is mainly determined by diffraction of light as explained by Bethe's aperture theory [26] and the resonant transmission caused by localized surface plasmons (LSPs) [11, 12, 27]. Optical transmission through metal nano-apertures can be further enhanced through the coupling of surface plasmon polaritons (SPPs) in a periodically corrugated metal film surrounding the aperture [10, 25, 28]. Similarly, periodic arrays of metal nano-apertures, usually referred to as metal nanohole arrays, also benefit from the coupling of SPPs to tunnel light through the nano-apertures with significantly boosted transmission, known as extraordinary optical transmission (EOT) [29].

Metal nano-apertures have proven very successful in optical trapping and sensing of individual nano-sized objects dispersed in liquids. Sensing of single proteins and DNA molecules down to a few nanometers have been demonstrated [15, 17–20, 30, 31]. When a dielectric nanoparticle is present inside the nano-aperture, optical transmission through the aperture increases because the particle makes the aperture optically larger by dielectric loading [15, 16]. Although metal nano-apertures have been extensively studied for sensing nanoparticles in liquids, they have not yet been investigated for sensing particles in aerosols. Furthermore, sensor configurations in which the analytes flow through metal nano-apertures have been demonstrated on plasmonic nanohole array sensors [32–34]; however, they have not been studied for airborne analytes, either.

To address aforementioned challenges and to break through the sizing limit of OPS-based techniques to effectively cover the size range of ultrafine particles, we propose a new sensor scheme referred to as a nano-optical particle sizer (NOPS), as shown in Fig. 1. Our scheme essentially implements a metal nano-aperture to boost the optical signals induced by ultrafine particles and to extend the sensing capabilities of metal nano-apertures into the realm of aerosols. The core component is an optical chip with a metal nano-orifice (MNO), comprised of a subwavelength

Fig. 1 Schematic of a nano-optical particle sizer (NOPS) based on a metal nano-orifice (MNO) for optical sizing of ultrafine particles (UFPs) in an aerosol
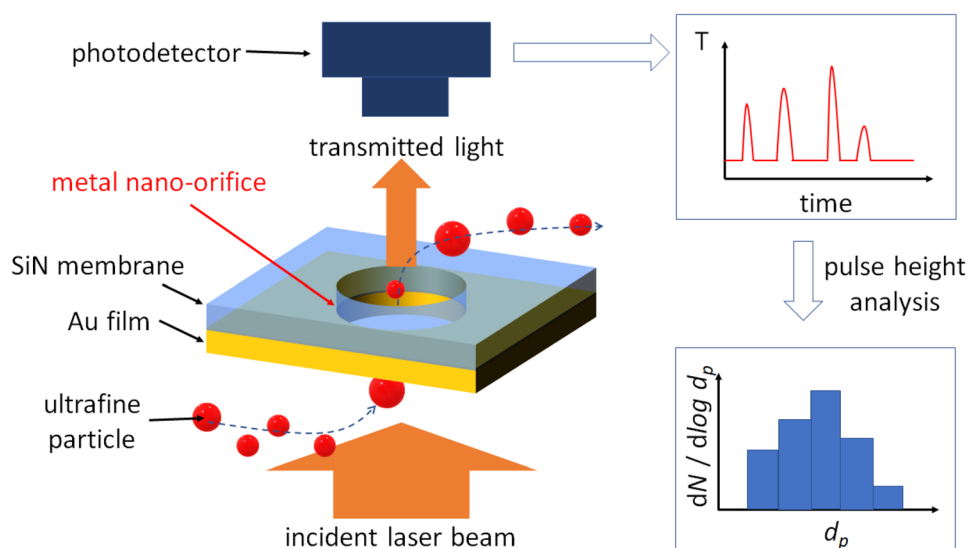
nano-aperture in a gold (Au) thin film on top of a holey silicon nitride (SiN) membrane. The nano-orifice extending through the bilayer of gold and silicon nitride film also serves as a nanofluidic channel for aerosol to flow through. The metal nano-aperture in gold film is the core optical sensing unit, while the silicon nitride membrane provides mechanical support for the gold film to ensure structural stability. A laser beam is focused onto the metal nano-orifice, and the transmitted light is detected by a photodetector. When an ultrafine particle travels through the metal nano-orifice, owing to the larger refractive index of the particle material than that of air in the background, the nano-orifice is "optically enlarged" by dielectric loading. The light transmission through the aperture will increase quickly to give a pulse in the acquired optical signal. The heights of pulses are correlated with the sizes of ultrafine particles, and the counts of pulses are interpreted into concentrations. Using pulse height analysis (PHA) on the signals, the particle size distributions of the ultrafine particles are attained.

In this work, we numerically studied the optofluidic properties and sensing responses of the proposed nano-optical particle sizer. Specifically, we simulated optical responses of metal nano-orifices for sizing ultrafine particles using finite difference time domain (FDTD). We also modeled the aerodynamic behaviors of ultrafine particles through the nano-orifice using finite element method (FEM) and particle tracing techniques. Furthermore, FDTD, FEM, and particle tracing were combined to simulate time-domain optical pulses induced by ultrafine particles. These numerical studies provide a theoretical framework for developing the proposed nano-optical particle sizer and for modeling optofluidic nanoplasmonic sensors towards aerosol applications.

Optical Responses of Metal Nano-Orifices

Finite Difference Time Domain Method

FDTD is a widely used numerical technique for simulating plasmonic nanostructures [35–45]. In this work, FDTD was implemented to simulate optical responses of metal nano-orifices by monitoring light transmission through
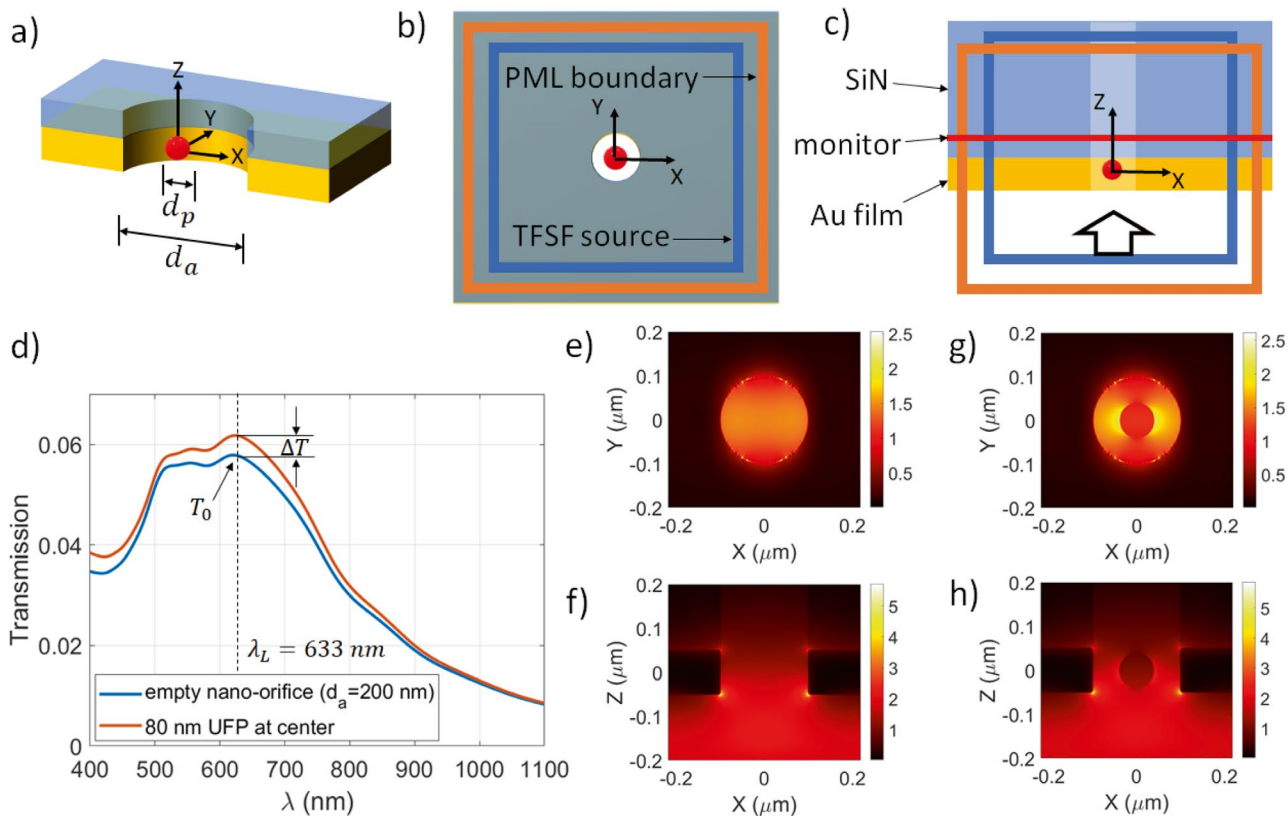

Fig. 2 FDTD simulation of a metal nano-orifice with 200 nm diameter. **a** Schematic view of the metal nano-orifice with an ultrafine particle at the center of the orifice. **b** Top-view (X-Y plane) and **c** side-view (X-Z plane) of the FDTD simulation configuration. The center of the nano-orifice in gold film is located at $X = Y = Z = 0$. **d** Simulated transmission spectrum of an empty nano-orifice and a nano-orifice with an 80 nm silica nanoparticle, showing T_0 and ΔT at the laser wavelength $\lambda_L = 633$ nm. **e** X-Y plane and **f** X-Z plane of simulated electric field enhancement mode profile at laser wavelength for the empty nano-orifice. **g** X-Y plane and **h** X-Z plane of simulated electric field enhancement mode profile at laser wavelength for the nano-orifice with the 80 nm silica nanoparticle at the center

the nano-orifice both with and without an ultrafine particle inside the aperture. FDTD simulations were carried out using the commercial package of Ansys Lumerical FDTD Solutions [46]. Figure 2a–c show schematics of the FDTD simulation configuration. The simulation model established in the software is shown in Supplementary Fig. S1. The metal nano-orifice is comprised of a 100 nm thick gold film and a silicon nitride cladding on top. The nano-orifice runs through both gold and silicon nitride films. The diameter of the nano-orifice is given by d_a. The material model used for gold follows Johnson and Christy's parameters [47], and the fitting of the material model is provided in Supplementary Fig. S2. The refractive index for silicon nitride is 2.0 and that of air is 1.0. The refractive index for the dielectric ultrafine particle is given by n_p. Spherical nanoparticles (NPs) composed of silica are used as the standard ultrafine particles in this study, and $n_p = 1.44$ (of silica) is used in the simulation by default. A plane wave (400 to 1100 nm wavelength, polarized along X direction) is launched using a total field scattered field (TFSF) source. The cross-section of the TFSF source in the X-Y plane is 600 nm × 600 nm. The launched wave propagates along +Z direction to transmit through the

metal nano-orifice, and the power spectrum of transmitted light is collected by a power monitor. Perfectly matched layers (PMLs) are used as the simulation boundaries. The gold film, the silicon nitride cladding, and the exit plane of the TFSF source all extend through the PMLs. The portions extended outside the PMLs are automatically truncated at the outer edge of PMLs by the software, and the overlap inside PMLs can minimize reflections from boundaries. The entire simulation is meshed using a uniform mesh of 1.5 nm, which was decided from a convergence study shown in Supplementary Fig. S3.

Figure 2d–h show the simulation results from a metal nano-orifice with diameter $d_a = 200$ nm. The simulated transmission spectra (transmission versus wavelength λ) in Fig. 2d compare the empty nano-orifice and the nano-orifice with an 80 nm silica nanoparticle at the center. With the nanoparticle inside the nano-orifice, the optical transmission increases distinctively due to dielectric loading, suggesting the capability of the metal nano-orifice in sensing ultrafine particles. Of particular interest is the simulated transmission at the laser wavelength λ_L. In this work, we consider the laser wavelength $\lambda_L = 633$ nm, to match the widely used 632.8 nm
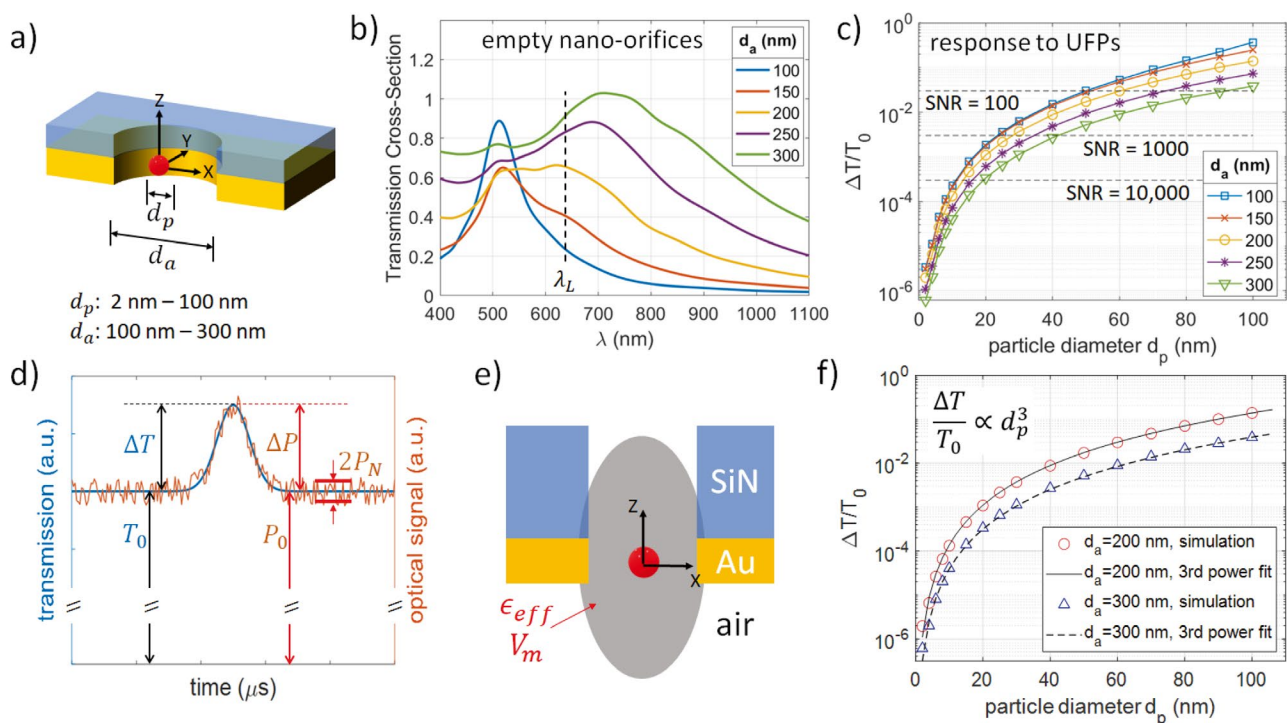
Fig. 3 Sensing responses of metal nano-orifices to an airborne silica nanoparticle located at the center of the metal nano-aperture. **a** Schematic of geometrical parameters studied in the simulations. **b** Transmission cross-section spectra for varying nano-aperture diameters, d_a from 100 to 300 nm. **c** Normalized transmission increment $\Delta\tilde{T} = \Delta T/T_0$ versus silica nanoparticle diameter d_p from 2 to 100 nm for each simulated nano-orifice. The black dashed horizontal lines mark the estimated detection threshold from an optical system with

SNR of 100, 1000, and 10,000 as indicated. **d** Schematic for the relations between the simulated transmission and the predicted optical signals. **e** Side-view schematic of an optical resonance mode in a metal nano-orifice with respect to the structure geometries. ϵ_{eff} is the effective dielectric constant of the equivalent medium, and V_m is the effective mode volume. **f** Fitting of simulated $\Delta T/T_0$ into 3rd power relations versus particle diameter

HeNe laser wavelength. The transmission of the empty orifice at λ_L is given by T_0, and the increment in transmission induced by the nanoparticle is given by ΔT. Figure 2e–h show the simulated mode profiles of electric field enhancement at λ_L. The field enhancement is defined as $|\vec{E}(\vec{r})|/E_0$, in which $|\vec{E}(\vec{r})|$ is the amplitude of the simulated electric field at location **r**, and E_0 is the amplitude of the electric field of the incident plane wave. These simulated mode profiles will be used to investigate the interaction between the nanoparticle and the light confined at the metal nano-orifice.

Sizing Limit of Metal Nano-Orifices

To numerically explore the potential of metal nano-orifices, sensing responses of ultrafine particles inside nano-orifices of different sizes were simulated, and the results are shown in Fig. 3. We studied d_a from 100 to 300 nm and d_p from 2 to 100 nm. The transmission spectra of empty metal nano-orifices shown in Fig. 3b were normalized according to the cross-sectional area of the TFSF source and the opening area of the orifice to give transmission cross-section [48]. As the nano-orifice gets larger, the transmission cross-section increases. For each nano-orifice, the transmission spectrum for an ultrafine particle located at the center of the metal nano-aperture was simulated. At laser wavelength λ_L, the transmission increment ΔT caused by the ultrafine particle was normalized with the transmission of empty nano-orifice T_0. Here, we introduce the definition of normalized transmission increment $\Delta \widetilde{T}$ given by $\Delta \widetilde{T} = \Delta T / T_0$, in order to compare the sensitivities of different metal nano-orifices. For all simulated metal nano-orifices, normalized transmission increments $\Delta \widetilde{T}$ are plotted against particle diameter d_p in Fig. 3c. The trends show that $\Delta \widetilde{T}$ has a third power dependence on d_p and a larger nano-orifice gives a lower sensitivity, which will be elucidated in detail in later sections.

The relation between the simulated transmission and the predicted optical signals acquired from an optical system is schematically illustrated in Fig. 3d. An optical pulse in the time domain is induced by one ultrafine particle, and the duration of the pulse is typically about a few microseconds, which will be studied in later sections. P_0 is the predicted optical power of light transmitted through an empty nano-orifice, while ΔP is the height of the optical pulse induced by the ultrafine particle. Since the optical power is proportional to transmission, we have $P_0 \propto T_0$ and $\Delta P \propto \Delta T$. The noise level in the optical signal is given by P_N. In order to distinguish an optical pulse from the noise, the height of the optical pulse must be at least three times the noise level, i.e., $\Delta P > 3P_N$. Therefore, the criteria to determine whether an ultrafine particle can be optically detected by the metal nano-orifice are given by $\Delta \widetilde{T} = \Delta T / T_0 = \Delta P / P_0 > 3P_N / P_0$. The signal-to-noise

ratio of the optical sytem is given by $SNR = P_0/P_N$. The criteria can thus be expressed as the following Eq. 1:

$$\Delta \widetilde{T} = \Delta T / T_0 > 3/SNR \tag{1}$$

The sizing limit, i.e., smallest detectable particle size, can be quantitatively determined based on Eq. 1. The horizontal dashed lines plotted in Fig. 3c mark the corresponding detection limit thresholds of $3/SNR$. If given an optical system with very high $SNR = 10,000$, all the simulated metal nano-orifices can reach a sizing limit of at least 20 nm, which can effectively extend the sizing limit of optical particle sizers into the range of ultrafine particles. If using an optical system with a lower SNR, the sizing limit will be negatively affected but is still much better than existing optical particle sizers. For example, if $SNR = 1000$, the sizing limit will become about 30 nm for $d_a = 200$ nm. It is noteworthy that, even if using an optical system with $SNR = 100$, a sizing limit of about 60 nm can still be attained for $d_a = 200$ nm, which is comparable to the performance of an advanced professional optical particle sizer based on a delicate intra-cavity laser [8].

Dielectric Loading of Ultrafine Particles

As a simplistic view, the sensing response of the metal nano-orifice can be interpreted based on dielectric loading in metal nano-apertures [15, 30]. As an approximation, the metal film can be treated as a perfect conductor. The nano-orifice can be considered as a nano-aperture immersed inside a homogeneous effective medium with an effective dielectric constant ϵ_{eff}. This effective dielectric constant is mode-dependent and, for simplicity, can be approximated as the spatial average of dielectric constant $\epsilon(\vec{r})$ weighted by the electric field intensity $|\vec{E}(\vec{r})|^2$ [49, 50]. ϵ_{eff} for the resonance mode of an empty nano-orifice can be given by:

$$\epsilon_{eff} = \frac{\int \epsilon(\vec{r}) |\vec{E}(\vec{r})|^2 d\vec{r}}{\int |\vec{E}(\vec{r})|^2 d\vec{r}} \tag{2}$$

From Bethe's aperture theory, the light transmission through the nano-aperture can be given by $T \propto \epsilon_{eff}^2$ [30]. When a dielectric nanoparticle is present inside the nano-orifice, located at $\vec{r}_p$, the effective dielectric constant is increased by $\Delta \epsilon_{eff}$, which causes an increase in transmission by ΔT.

The normalized transmission increment $\Delta \widetilde{T}$ is thus given by

$$\Delta \widetilde{T} = \frac{\Delta T}{T_0} = \frac{2\Delta \epsilon_{eff}}{\epsilon_{eff}} \tag{3}$$

The dielectric constant of the nanoparticle material is ϵ_p and $\epsilon_p = n_p^2$. The dielectric constant of air is given by $\epsilon_0 = n_0^2 = 1$. The dielectric nanoparticle has a volume of V_p, and its presence

at $\vec{r}_p$ essentially increases the dielectric constant from air ϵ_0 into ϵ_p, by a volume of V_p. As a perturbation in first order, $\Delta\epsilon_{eff}$ can be approximately given by

$$\Delta\epsilon_{eff} = \frac{V_p(\epsilon_p - \epsilon_0)|\vec{E}(\vec{r}_p)|^2}{\int |\vec{E}(\vec{r})|^2 d\vec{r}} \quad (4)$$

Substitution of Eqs. 2 and 4 into Eq. 3 gives

$$\Delta\widetilde{T} = \frac{\Delta T}{T_0} = 2V_p(\epsilon_p - \epsilon_0)\frac{|\vec{E}(\vec{r}_p)|^2}{\int \epsilon(\vec{r})|\vec{E}(\vec{r})|^2 d\vec{r}} \quad (5)$$

The light confinement in the nano-orifice can be described by an effective mode volume, V_m, defined as

$$V_m = \frac{\int \epsilon(\vec{r})|\vec{E}(\vec{r})|^2}{\epsilon(\vec{r}_c)|\vec{E}(\vec{r}_c)|^2} = \frac{\int \epsilon(\vec{r})|\vec{E}(\vec{r})|^2}{\epsilon_0|\vec{E}(\vec{r}_c)|^2} \quad (6)$$

where $\vec{r}_c$ is the position of the antinode of the resonance mode (usually the maxima of the electric field intensity), and $|\vec{E}(\vec{r}_c)|^2$ is the electric field intensity at the antinode. In our configuration, the antinode is located in air, and therefore, $\epsilon(\vec{r}_c) = \epsilon_0 = 1$.

Substitution of Eq. 6 into Eq. 5 gives

$$\Delta\widetilde{T} = \frac{\Delta T}{T_0} = \frac{2(\epsilon_p - \epsilon_0)}{\epsilon_0}\frac{V_p}{V_m}\frac{|\vec{E}(\vec{r}_p)|^2}{|\vec{E}(\vec{r}_c)|^2} \quad (7)$$

For a spherical nanoparticle, $V_p = \pi d_p^3/6$,

$$\Delta\widetilde{T} = \frac{\pi(\epsilon_p - \epsilon_0)d_p^3}{3\epsilon_0 V_m}\frac{|\vec{E}(\vec{r}_p)|^2}{|\vec{E}(\vec{r}_c)|^2} = \frac{\pi(n_p^2 - n_0^2)d_p^3}{3n_0^2 V_m}\frac{|\vec{E}(\vec{r}_p)|^2}{|\vec{E}(\vec{r}_c)|^2} \quad (8)$$

Equations 7 and 8 suggest that the normalized transmission increment is proportional to the particle's volume and has a 3rd power dependence on the particle diameter. To validate this relation, in Fig. 3f, the simulated results for metal nano-orifice with $d_a = 200$ nm and $d_a = 300$ nm were nicely fitted into the third power equation versus the particle diameter d_p. The values of V_m obtained from the fits are 0.0081 μm^3 for $d_a = 200$ nm and 0.0288 μm^3 for $d_a = 300$ nm. These values are consistent with the mode profiles simulated from these two metal nano-orifices. According to Eq. 7, a metal nano-orifice with a smaller mode volume V_m, i.e., stronger field confinement, has a higher sensitivity for sizing ultrafine particles. This trend is consistent with the simulation results shown in Fig. 3c and f, in which a smaller metal nano-orifice indeed gives a higher sensitivity.

The superb sensitivity of metal nano-orifices for sizing ultrafine particles stems from the 3rd power dependence of the induced optical signal on the particle diameter, as demonstrated in Fig. 3f. In contrast, for optical particle

sizers based on conventional optics, as the particle diameter scales down below 100 nm, the intensity of scattered light decreases sharply, due to the dominating Rayleigh scattering in this particle size range [4]. As shown in Supplementary Fig. S4, the intensity of scattered light ΔI has a 6th power dependence on the particle diameter for ultrafine particles, i.e., $\Delta I \propto d_p^6$. In comparison, the metal nano-orifice has a much slower decrease (3rd power) in $\Delta\widetilde{T}$ as the particle size decreases, which gives much stronger optical signals than Rayleigh scattering and hence enables effective optical sizing of ultrafine particles.

Location-Dependent Sensing Responses

Equation 5 suggests that the normalized transmission increment $\Delta\widetilde{T}$ is proportional to the electric field intensity at the particle's location. In previous sections, the ultrafine particles were fixed at the center of the nano-orifice. Considering the actual dynamic process to measure an ultrafine particle when it travels through a metal nano-orifice, the optical response at any given moment depends on the location of the particle. Brownian motions of particles introduce randomness into the particles' trajectories, which will cause uncertainties in the optical signals. Studying the location-dependent optical responses can reveal the uncertainty in determing the particle size which is related to the resolution in sizing ultrafine particles.

Out of all metal nano-orifices simulated in previous sections, we chose $d_a = 200$ nm to continue our investigation. This is a rational choice, considering the sensitivity, the practical nanofabrication resolution, and the fluidic resistance for the aerosol flow. A smaller nano-orifice is optically more sensitive for sizing ultrafine particles, but the challenges in nanofabrication and the fluidic resistance both increase abruptly as the orifice decreases in size. We simulated the location-dependent optical responses from the metal nano-orifice with $d_a = 200$ nm. For each simulation, a silica nanoparticle with $d_p = 20$ nm was introduced into the nano-orifice at a different location along the most representative X-Z and X-Y planes.

Figure 4a shows the simulated $\Delta\widetilde{T}$ as the silica nanoparticle's position was swept vertically along the center Z axis ($X = Y = 0$). When the particle is located about 200 nm away from the gold film, either below or above the film, $\Delta\widetilde{T}$ is nearly zero which resembles an empty nano-orifice. This is consistent with the near-field of the resonance mode localized at the metal nano-orifice. The peak transmission occured at about 25 to 50 nm below the center of the gold film. This observation is consistent with the simulated vertical-plane field profile shown in Fig. 2f. Due to the sharp corners at the bottom edges of the gold nano-orifice established in the simulation, the electric field enhancement "hot spots" are closer to the bottom side of the gold film. As a result, the

Fig. 4 Effects of the location of a silica nanoparticle with $d_p = 20$ nm in a plasmonic nano-orifice with $d_a = 200$ nm. **a** Simulated $\Delta \widetilde{T} = \Delta T/T_0$ for sweeping the particle location along the center Z axis ($X = Y = 0$). **b** Simulated $\Delta \widetilde{T} = \Delta T/T_0$ for sweeping the particle location inside the X-Y plane located at the center of the orifice ($Z = 0$). The blue dashed circle marks the geometry of the orifice
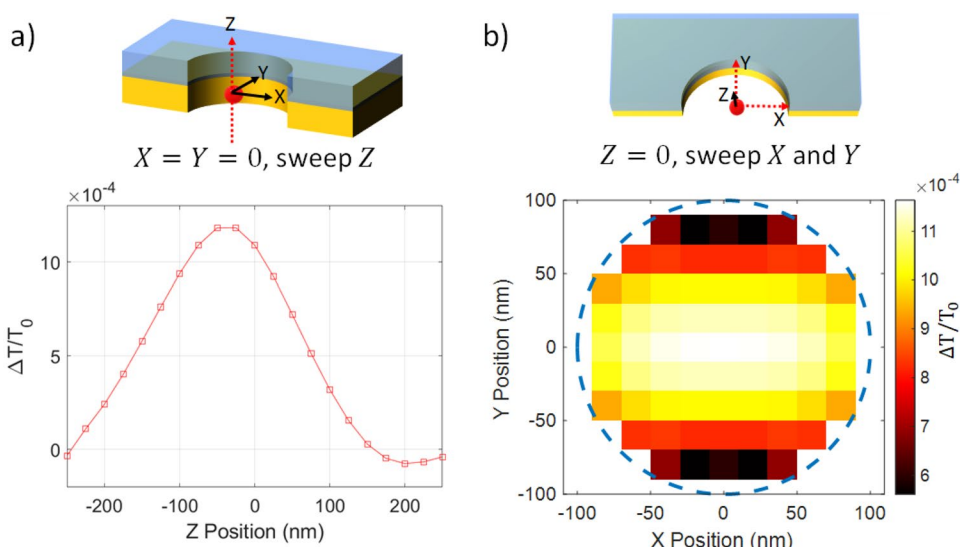
simulated $\Delta \widetilde{T}$ reaches the peak at a location closer to the bottom of the nano-orifice. It should be noted that the peak value of $\Delta \widetilde{T}$ differs very little from the value at $Z = 0$ nm. In addition, in practical physical devices of gold nano-orifices, the corners have much smoother curvatures than what was modeled in simulations. Therefore, we still consider the simulation results from the center of gold film ($Z = 0$ nm) as the standard for predicting the height of optical pulses induced by ultrafine particles, such as the result shown in Fig. 3c for studying the sizing limit.

Figure 4b shows a 2-D map of simulated $\Delta \widetilde{T}$ as the particle's position was swept horizontally along the center plane of the metal nano-orifice ($Z = 0$). The value of $\Delta \widetilde{T}$ varies from 5.6×10^{-4} to 11.6×10^{-4}. The peak value stays consistent for the particle located -50 nm $\leq Y \leq +50$ nm with very little variation. For the two spots at the top and bottom of the circle, $\Delta \widetilde{T}$ decreases into a lower value. This variation is a result of the inhomogenous field enhancement inside the metal nano-orifice, as can be observed from Fig. 2e. Specifically, the field enhancement profile has two relatively weaker spots at the top and bottom of the circle. This phenomenon results from the dipolar resonance of the localized surface plasmons excited by the X-polarized incident wave. Since the metal nano-orifice tells the size of a particle based on the value of $\Delta \widetilde{T}$, this variation will introduce uncertainty in the particle size which will affect the resolution for sizing ultrafine particles. Based on the results in Fig. 3c and Fig. 4b, the magnitude of this location-dependent variation will lead to an uncertainty in determining the particle diameter by about 5 nm when sizing a 20 nm silica nanoparticle. It should be noted that, since this variation results from using linearly polarized light, it can be significantly reduced if a circularly-polarized laser beam is implemented to probe the metal nano-orifice.

Dynamic Optofluidic Responses of Metal Nano-Orifices

For nanoplasmonic sensors, there are mainly two modes for introducing analytes into the sensor stuctures: flow-over and flow-through [32–34, 51–53]. In the majority of existing sensors, analytes are introduced by flowing over the sensor structure. In comparison, in the flow-through mode, the analytes flow through nanofluidic channels formed by nano-apertures, which has proven to be more advantageous for certain applications [32–34, 54]. It is noteworthy that the flow-through configuration has not yet been investigated for sensing aerosols.

The functioning mechanism of the proposed nano-optical particle sizer relies on aerosol flow through the metal nano-orifice, which acts as a nanofluidic channel for the aerosol. For the flow-through configuration, the aerodynamic behaviors of ultrafine particles traveling through the metal nano-orifice will have direct impacts on the optical signals. Finite element method (computational fluid dynamics (CFD) module) and particle tracing module from COMSOL Multiphysics [55] were implemented to compute the trajectories of ultrafine particles traveling through a metal nano-orifice. Based on the time-dependent particle locations given by the trajectories, dynamic optical responses were simulated using FDTD.

Modeling of UFPs' Trajectories

The modeling of trajectories of ultrafine particles shown in Fig. 5a and b was carried out in a two-step procedure. In the first step, the CFD module was implemented to simulate the steady-state air flow through the nanofluidic channel by solving the pressure and fluid velocity fields. In the second step, the particle tracing module was used
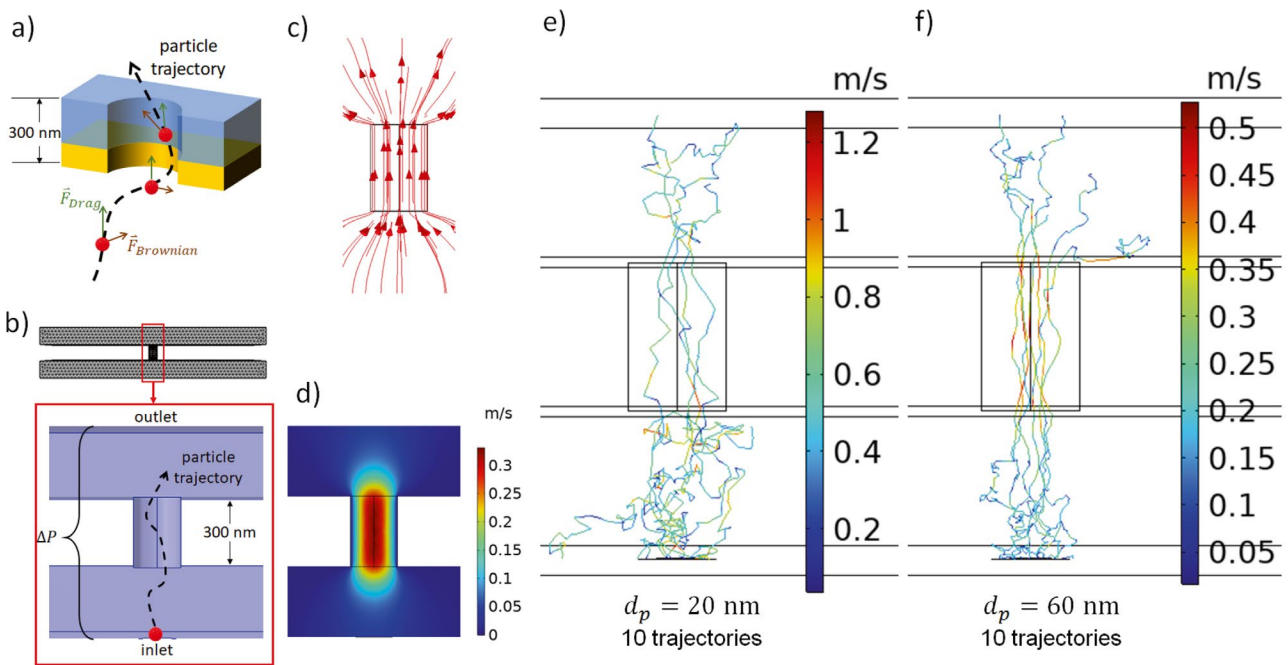
Fig. 5 Simulated trajectories of ultrafine particles traveling through a metal nano-orifice with $d_a = 200$ nm. **a** Schematic for the trajectories of ultrafine particles under the drag force and Brownian force. **b** Simulation configuration for laminar air flow through the nano-orifice driven by a differential pressure $\Delta P = 1$ kPa. **c** Streamline plot of the simulated fluid velocity field $\vec{u}$ at the nano-orifice. **d** Color map of the magnitude of fluid velocity, $|\vec{u}|$. Simulated trajectories of 10 silica nanoparticles with **e** $d_p = 20$ nm and **f** $d_p = 60$ nm, which were released from the center of the inlet. The magnitude of particle velocity, $|\vec{v}|$, is given by the color bar

to simulate time-dependent trajectories of ultrafine particles based on the forces applied on the particles. In our model, air is treated as a steady-state, homogeneous, Newtonian, incompressible fluid governed by the continuity and Navier–Stokes equations. For our application dealing with low pressure and low fluid velocity, the incompressible fluid model gives sufficient accuracy [56].

As shown in Fig. 5a and b, the simulation geometry of the metal nano-orifice was defined as a cylindrical nanochannel in a membrane with thickness of 300 nm, to account for the 100 nm-thick gold film and a 200 nm-thick SiN cladding film. d_a was chosen to be 200 nm, for investigating the correlations with previous FDTD simulations of the same nano-orifice size. The inlet and outlet were modeled as two bulky channels with a cross section of 5 μm × 5 μm, which are much larger than the nano-orifice, such that the simulation can closely approximate the nano-orifice channeling between two bulk aerosol chambers. A no-slip boundary condition was applied to all walls except the inlet and outlet. A static differential pressure ΔP was applied between the inlet and outlet boundaries. Based on simulations of a nano-optical particle sizer configuration shown in Supplementary Fig. S6, $\Delta P = 1$ kPa was found to be a reasonable cross-membrane pressure to be applied across the nano-orifice. A physics-controlled fine mesh was implemented for both the CFD and particle tracing modules.

The degree of turbulence of an aerosol flow is governed by the Reynold's number:

$$Re = \frac{\rho_{air} U L}{\mu_{air}} \tag{9}$$

in which the characteristic length $L \approx 5$ μm (given by the cross section of inlet and outlet), the density of air $\rho_{air} = 1.204$ kg/m^3, and the dynamic viscosity of air $\mu_{air} = 1.825 \times 10^{-5}$ $kg/(m \cdot s)$. The flow velocity U was estimated to be no more than 1 m/s, and the calculated Reynold's number is at most 0.28. Due to the very small Reynold's number, the flow is considered laminar in nature, and therefore, a laminar flow model was used in the simulation.

From the steady-state laminar flow simulation, the pressure and fluid velocity field $\vec{u}$ were solved for the nano-orifice. The streamline plot of the simulated fluid velocity field $\vec{u}$ across the nano-orifice is shown in Fig. 5c. The color map of the magnitude of fluid velocity, $|\vec{u}|$, at X-Z cross section is shown in Fig. 5d. The maximum fluid velocity is around 0.33 m/s under the 1 kPa differential pressure.

In the particle tracing module, individual ultrafine particles were released from the center of the inlet, located 300 nm away from the nano-orifice. At each time step (given by Δt), the particle's location was computed and updated to give a time-dependent particle trajectory. At any given time

step, the particle's velocity $\vec{v}$ was calculated from the total forces acting on the particle, based on Newton's second law:

$$m_p \frac{d\vec{v}}{dt} = \vec{F}_{Drag} + \vec{F}_{Brownian} \tag{10}$$

in which m_p is the particle's mass, $\vec{F}_{Drag}$ is the drag force, and $\vec{F}_{Brownian}$ is the Brownian force, as shown in Fig. 5a. For simulating the trajectories of ultrafine particles, drag force and Brownian force are the two dominating forces. Other forces are negligible and are not considered in this work. For example, gravitational force for ultrafine particles has very little effect on the particle trajectory due to the very small mass of the particles. Electrostatic forces are not included in the simulation because ultrafine particles in a practical aerosol particle sizer device are usually first processed with an aerosol neutralizer and are therefore neutral in electric charge. In the computation, each ultrafine particle is treated as a dimensionless point-like particle with a particle mass m_p, which is defined by the particle diameter d_p and particle material density ρ_p. From the particle velocity $\vec{v}$ solved at each time step, the particle's location is updated correspondingly to construct a particle trajectory.

Drag force is the force acting on the particle opposite to the relative motion between the particle and the surrounding fluid. Drag force is dependent on the simulated steady-state fluid velocity field $\vec{u}$, particle's velocity $\vec{v}$, particle mass m_p, and particle velocity response time τ_p, given by

$$\vec{F}_{Drag} = \frac{m_p(\vec{u} - \vec{v})}{\tau_p} \tag{11}$$

The value of τ_p depends on the type of drag law being applied, which was determined by the relative Reynold's number

$$Re_r = \frac{\rho_{air}|\vec{u} - \vec{v}|d_p}{\mu_{air}} \tag{12}$$

For ultrafine particles in an aerosol flow driven by a low differential pressure, $Re_r << 1$, and the Stokes drag law was chosen, which gives

$$\tau_p = \frac{\rho_p d_p^2}{18\mu_{air}} \tag{13}$$

where ρ_p is the particle material density. For silica nanoparticles, $\rho_p = 2,650\ kg/m^3$.

Random Brownian motions of ultrafine particles were simulated by applying the random Brownian forces on the particle, given by

$$\vec{F}_{Brownian} = (\zeta_x \hat{x} + \zeta_y \hat{y} + \zeta_z \hat{z})\sqrt{\frac{6\pi k_B \mu_{air} T d_p}{\Delta t}} \tag{14}$$

where T is the absolute temperature of the aerosol (room temperature used in this work), k_B is the Boltzmann constant, and ζ_x, ζ_y, and ζ_z are normally distributed random numbers with a mean of zero and unit standard deviation. It should be noted that, ζ_x, ζ_y, and ζ_z are independent from each other.

As seen in Eq. 14, the Brownian force is strongly dependent on the particle size. For ultrafine particles which have very large surface-to-volume ratio, Brownian force plays a crucial role on the particle trajectories [4]. Supplementary Fig. S5 compares the effects of Brownian forces on the simulated particle trajectories of ultrafine particles. The speading and randomization of particle trajectories can only be correctly computed when Brownian force is included.

Figure 5e and f show particle trajectories of 10 silica nanoparticles for $d_p = 20$ nm and $d_p = 60$ nm, respectively. The colors on the trajectories correspond to the magnitude of the particle velocity, $|\vec{v}|$, specified by the color bar. These ultrafine particles were all released from the center of the inlet. The time-dependent study was solved from 0 to 10 μs with a time step $\Delta t = 0.1\ \mu$s. It should be noted that these simulated trajectories should be viewed as independent particle trajectories that are assembled together to show the collective effects for the particle size of interest. The interactions among ultrafine particles are not included in our simulations, and the particle trajectories are therefore independent from each other. In the practical operation of a nano-optical particle sizer, the particle concentrations are relatively low, and there is a very low probability for multiple ultrafine particles to be present inside the nanofluidic channel simultaneously. Consequently, the interactions among particles were neglected when simulating the trajectories.

Due to the Brownian motions, the particle trajectories have severe randomness and appear chaotic. As a result, not all particles traveled through the nano-orifice by the end of the simulated period. When comparing the 10 trajectories for $d_p = 20$ nm and $d_p = 60$ nm, the former group (smaller particles) has a lower ratio for the particles traveling through the nano-orifice, because the Brownian motions are more significant for smaller particles. In addition, smaller particles in general have larger particle velocity magnitudes, also partially resulting from the stronger Brownian motions.

Simulation of Dynamic Optical Responses

The finite element method (CFD module), particle tracing, and FDTD as three subsequent steps can be combined into one powerful computation tool for studying the time-domain dynamic optofluidic response of the metal nano-orifice to ultrafine particles in an aerosol driven by a cross-membrane pressure across the nanofluidic channel. The

particle trajectories computed from finite element method and particle tracing provide the particle's time-dependent locations, which allows the particle-induced optical response to be simulated by FDTD. Individual particle trajectories were extracted, and the particle locations were loaded into FDTD to simulate the time-dependent dynamic optical response, defined as $\Delta \widetilde{T} = \Delta T / T_0$ as a function of time. One FDTD simulation was run for each particle location.

Figure 6a shows two extracted particle trajectories, one for $d_p = 20$ nm and the other for $d_p = 60$ nm. The dynamic optical response simulated by FDTD is shown in Fig. 6b and c, for $d_p = 20$ nm and $d_p = 60$ nm, respectively. The simulated dynamic optical responses provide realistic predictions on optical signals that can be acquired from the metal nano-orifice. After being released, when the particle is far from the nano-orifice, $\Delta \widetilde{T}$ is nearly zero. When the particle is present inside the metal nano-orifice, a strong increase in $\Delta \widetilde{T}$ is induced. As the particle leaves the nano-orifice, $\Delta \widetilde{T}$ decreases into nearly zero again. Clearly, each ultrafine particle traveling through the metal nano-orifice will generate an optical pulse in $\Delta \widetilde{T}$. The pulse heights of the simulated optical signals, about 10^{-3} for $d_p = 20$ nm and about 0.03 for $d_p = 60$ nm, are consistent with the FDTD simulation results in Fig. 3c. The pulse width is in the range of 1 to 1.5 μs, which suggests that a sampling rate of 10 Msps (million

samples per second) can be an appropriate configuration for digitizing the pulsatile optical signals.

The bandwidth of the optical signal plays an important role for determining the required performance characteristics of the optical system. The frequency-domain spectra of the simulated optical responses were calculated using fast Fourier transform (FFT). The number of data points attained from simulations ranges from 20 to 40, depending on the trajectories of the particles. The data points were padded with zeros to make the overall data length reach 400, which can significantly increase frequency resolution in the spectrum. The zero padding was implemented because when the particles are away from the nano-orifice, the optical signal $\Delta \widetilde{T}$ is very low and can be treated as zero. After zero padding, the data was processed with the FFT function in MATLAB. A sampling frequency of 10 MHz was used due to the 0.1 μs time step used in the COMSOL simulations. The frequency-domain spectra for $d_p = 20$ nm and $d_p = 60$ nm are given in Fig. 6d and e, respectively. The smaller particle's signal has a larger bandwidth than bigger particles. The smaller particle has an overall larger magnitude of particle velocity and a more chaotic particle trajectory due to more significant Brownian motion, which lead to more abrupt changes in optical transmission and therefore a stronger high-frequency component. The frequency-domain analysis suggests that
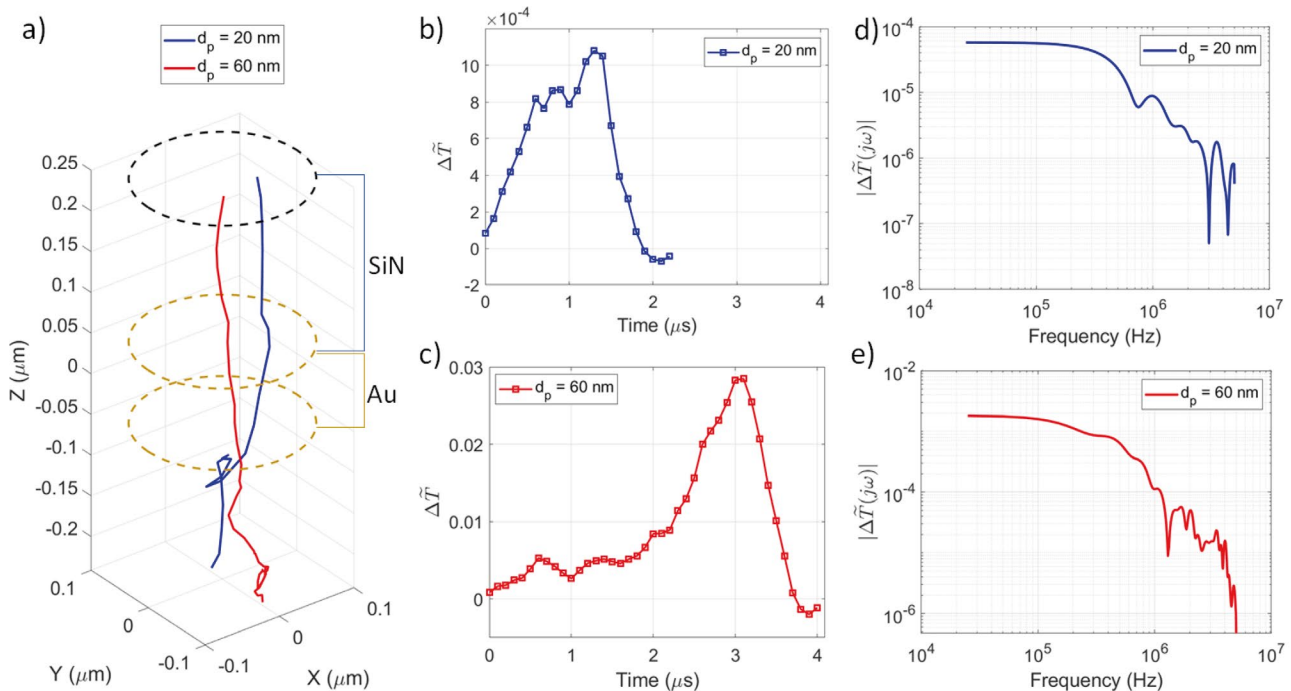
Fig. 6 Dynamic optofluidic response of ultrafine particles traveling through a metal nano-orifice with $d_a = 200$ nm. **a** Extracted single particle trajectory of a silica nanoparticle for $d_p = 20$ nm and $d_p = 60$ nm. The dashed circles are the outlines of the nano-orifice.

FDTD simulation results of $\Delta \widetilde{T} = \Delta T / T_0$ as a function of time for **b** $d_p = 20$ nm and **c** $d_p = 60$ nm. Frequency-domain spectrum of the simulated dynamic optical response for **d** $d_p = 20$ nm and **e** $d_p = 60$ nm

the particle size determined from the pulse height of $\Delta\widetilde{T}$ can potentially be validated by the Fourier transform of the acquired optical signal. For either case of the simulated particle size, the bandwidth (defined as -20 dB magnitude in this work) is no more than 2 MHz.

Discussion

In this work, we focus on the performance characteristics of single metal nano-orifices. One potential drawback of a single metal nano-orifice is the limited aerosol flow due to the high fluidic resistance through such a nanofluidic channel. For practical applications, the single metal nano-orifice is suitable for sampling and analyzing a very small portion of the provided aerosol, and it would be advantageous to be integrated with compact aerosol sampling devices, such as lab-on-chip microfluidic aerosol separators and samplers [57]. One potential solution to the fluidic resistance is to incoporate many metal nano-orifices into one optical chip to enhance the aerosol flow by many folds and probe all orifices simultaneously with imaging-based detection. A similar strategy using a gold nanodisk array and an electron-multiplied charge-coupled device has been demonstrated for detecting and sizing dielectric nanoparticles in a liquid [58].

Due to Brownian diffusion, the nanoparticles have random and chaotic trajectories, which introduce uncertainties into the measurement. Firstly, Brownian diffusion will affect the sampling efficiency of nanoparticles, defined as the percentage of nanoparticles that can enter the nano-orifice. The sampling efficiency depends on the nano-orifice geometry, the pressure across the nano-orifice, the nanoparticle size, and the distance from the entrance of the nano-orifice. Supplementary Fig. S8 shows simulated trajectories of silica nanoparticles launched at various distances from the entrance of the nano-orifice. In each simulation, 1000 particle trajectories were simulated, and the number of particles entering the nano-orifice was counted using a freezing boundary at the outlet. The sampling efficiencies for different particle sizes and launching distances are listed in Supplementary Table S1. When launched at the same distance, particles with 20 nm diameter have a lower sampling efficiency than particles of 60 nm diameter. If there were no Brownian force, all particles would have been driven by the drag force of the flow to enter the nano-orifice, as shown in Supplementary Fig. S5(a). Due to the Brownian force in reality, particles' trajectories are dispersed into all random directions, and a portion of particles will not enter the nano-orifice. Smaller particles are under stronger effects of Brownian diffusion and thus have a lower sampling efficiency. For particles launched closer to the nano-orifice, the sampling efficiency is higher, because the drag force is stronger near the nano-orifice. These trends suggest that the metal nano-orifice mainly measures nanoparticles flowing near the nano-orifice. For practical applications, the calibration of NOPS must take the sampling efficiency into account, which will be investigated in our future work.

Secondly, due to Brownian diffusion, when a nanoparticle is traveling inside the nano-orifice and crossing the center plane of the gold film, it can be at any position on that plane. The simulation results of X-Y position sweep in Fig. 4 showed very small variations in the optical signal, despite the inhomogeneous field profile excited by X-polarized light (shown in Fig. 2). This signal variation can cause uncertainty by about 5 nm when sizing a 20 nm silica nanoparticle, which is still satisfactory considering the challenges in sizing such small nanoparticles. The simulated dynamic optical pulses shown in Fig. 6 further confirmed the consistency of the optofluidic responses. Although the particle trajectories can vary widely, the peaks of the optical pulses can still stay consistent.

There may be concerns about practical applications of the metal nano-orifice when measuring polydisperse particles in aerosols, which have a range of particle sizes, versus well-defined monodisperse particles that have a single discrete particle size. It should be noted that our nano-optical particle sizer is an individual-type particle counter, which measures one particle at a time. For regular measurements, the particle concentrations are relatively low, and there is a low probability for coincidence events for multiple ultrafine particles to be present inside the nanofluidic channel simultaneously. For most particles, each particle will trigger an individual optical pulse. The optical signals from smaller particles will not be affected by those from bigger particles because their triggered optical pulses are separated in time domain. In practical applications, to accurately size the particles, the optical system should be calibrated with high quality monodisperse particles to attain a calibration curve. After calibration, any ensemble of polydisperse particles with varying sizes can be accurately detected owing to the relationship between pulse height and particle size.

Conclusion

The metal nano-orifice introduced in this work is a novel scheme for aerosol particle sizing based on optical transmission of a nano-aperture in a metal film. The feasibility of the metal nano-orifice was numerically studied using finite element method, particle tracing, and finite difference time domain, which were combined to compute the dynamic optofluidic responses. The numerical results predicted that airborne particles in the ultrafine size range can be effectively sized through a metal nano-orifice. With an optical

system of very high signal-to-noise ratio, silica nanoparticles as small as 20 nm in diameter can potentially be measured. Even with a lower signal-to-noise ratio, silica nanoparticles as small as 60 nm can still be measured, which is comparable to the performance of an advanced professional optical particle sizer based on a delicate intra-cavity laser. The metal nano-orifice shows great promise for real-time sensing of ultrafine particles and may open up new avenues in nanoplasmonics-based aerosol sensing applications for health solutions.

Appendix. List of Symbols

d_a	Diameter of the nano-orifice
d_p	Diameter of the nanoparticle
E_0	Amplitude of the electric field of the incident plane wave
$|\vec{E}(\vec{r})|$	Amplitude of the simulated electric field at location $\vec{r}$
ΔT	Transmission increment caused by the ultrafine particle
T_0	Transmission of an empty nano-orifice
$\Delta \widetilde{T}$	Normalized transmission increment
P_0	Optical power of light transmitted through empty nano-orifice
ΔP	Height of the optical pulse induced by the ultrafine particle
P_N	Noise level in the optical signal
ϵ_{eff}	Effective dielectric constant
$\epsilon(\vec{r})$	Material dielectric constant at location $\vec{r}$
n_0	Refractive index of air
ϵ_p	Dielectric constant of nanoparticle material
ϵ_0	Dielectric constant of air
n_p	Refractive index of nanoparticle material
V_p	Volume of dielectric nanoparticle
V_m	Effective mode volume
$\vec{r}_p$	Position of dielectric nanoparticle
$\vec{r}_c$	Position of the antinode of the resonance mode
ρ_{air}	Density of air
μ_{air}	Dynamic viscosity of air
U	Flow velocity of the fluid
L	Characteristic width of the fluidic channel cross section
$\vec{u}$	Fluid velocity field
$\vec{v}$	Particle velocity
m_p	Particle mass
τ_p	Particle velocity response time
ρ_p	Density of the particle material
T	Absolute temperature of the aerosol
ζ	Random number in normal distribution
k_B	Boltzmann constant

Declarations

Ethics Approval Not applicable.

Consent to Participate Not applicable.

Consent for Publication All authors accepted.

Competing Interests The authors declare no competing interests.

References

1. Schraufnagel DE (2020) The health effects of ultrafine particles. Exp Mol Med 52(3):311–317. https://doi.org/10.1038/s12276-020-0403-3
2. Kwon HS, Ryu MH, Carlsten C (2020) Ultrafine particles: unique physicochemical properties relevant to health and disease. Exp Mol Med 52(3):318–328. https://doi.org/10.1038/s12276-020-0405-1
3. Downward GS, van Nunen EJ, Kerckhoffs J et al (2018) Long-term exposure to ultrafine particles and incidence of cardiovascular and cerebrovascular disease in a prospective study of a dutch cohort. Environ Health Perspect 126(12):127007. https://doi.org/10.1289/ehp3047
4. Xu R (2001) Particle characterization: light scattering methods, vol 13. Springer Science & Business Media. https://doi.org/10.1007/0-306-47124-8
5. Clarke A, Porter J, Valero F et al (1996) Vertical profiles, aerosol microphysics, and optical closure during the Atlantic stratocumulus transition experiment: measured and modeled column optical properties. J Geophys Res-Atmos 101(D2):4443–4453. https://doi.org/10.1029/95JD03140
6. Clarke AD, Ahlquist NC, Howell S et al (2002) A miniature optical particle counter for in situ aircraft aerosol research. J Atmos Oceanic Tech 19(10):1557–1566. https://doi.org/10.1175/1520-0426(2002)019⟨1557:AMOPCF⟩2.0.CO;2
7. Gao R, Perring A, Thornberry T et al (2013) A high-sensitivity low-cost optical particle counter design. Aerosol Sci Technol 47(2):137–145. https://doi.org/10.1080/02786826.2012.733039
8. TSI Laser Aerosol Spectrometer (LAS) 3340A (2023). https://tsi.com/products/particle-sizers/particle-size-spectrometers/laser-aerosol-spectrometer-3340a/

9. Pan M, Lednicky JA, Wu CY (2019) Collection, particle sizing and detection of airborne viruses. J Appl Microbiol 127(6):1596–1611. https://doi.org/10.1111/jam.14278

10. Lezec HJ, Degiron A, Devaux E et al (2002) Beaming light from a subwavelength aperture. Science 297(5582):820–822. https://doi.org/10.1126/science.1071895

11. Barnes WL, Dereux A, Ebbesen TW (2003) Surface plasmon subwavelength optics. Nature 424(6950):824–830. https://doi.org/10.1038/nature01937

12. Degiron A, Lezec H, Yamamoto N et al (2004) Optical transmission properties of a single subwavelength aperture in a real metal. Opt Commun 239(1):61–66. https://doi.org/10.1016/j.optcom.2004.05.058

13. Genet C, Ebbesen TW (2007) Light in tiny holes. Nature 445(7123):39–46. https://doi.org/10.1038/nature05350

14. Brolo AG, Gordon R, Leathem B et al (2004) Surface plasmon sensor based on the enhanced light transmission through arrays of nanoholes in gold films. Langmuir 20(12):4813–4815. https://doi.org/10.1021/la0493621

15. Gordon R (2019) Biosensing with nanoaperture optical tweezers. Opt Laser Technol 109:328–335. https://doi.org/10.1016/j.optlastec.2018.07.019

16. Juan ML, Gordon R, Pang Y et al (2009) Self-induced back-action optical trapping of dielectric nanoparticles. Nat Phys 5(12):915–919. https://doi.org/10.1038/nphys1422

17. Pang Y, Gordon R (2011) Optical trapping of 12 nm dielectric spheres using double-nanoholes in a gold film. Nano Lett 11(9):3763–3767. https://doi.org/10.1021/nl201807z

18. Chen C, Juan ML, Li Y et al (2012) Enhanced optical trapping and arrangement of nano-objects in a plasmonic nanocavity. Nano Lett 12(1):125–132. https://doi.org/10.1021/nl2031458

19. Pang Y, Gordon R (2012) Optical trapping of a single protein. Nano Lett 12(1):402–406. https://doi.org/10.1021/nl203719v

20. Zehtabi-Oskuie A, Jiang H, Cyr BR et al (2013) Double nanohole optical trapping: dynamics and protein-antibody co-trapping. Lab Chip 13:2563–2568. https://doi.org/10.1039/C3LC00003F

21. Kim JD, Lee YG (2014) Trapping of a single DNA molecule using nanoplasmonic structures for biosensor applications. Biomed Opt Express 5(8):2471–2480. https://doi.org/10.1364/BOE.5.002471

22. Reilly TH, Chang SH, Corbman JD et al (2007) Quantitative evaluation of plasmon enhanced Raman scattering from nanoaperture arrays. J Phys Chem C 111(4):1689–1694. https://doi.org/10.1021/jp066802j

23. Djaker N, Hostein R, Devaux E et al (2010) Surface enhanced Raman scattering on a single nanometric aperture. J Phys Chem C 114(39):16250–16256. https://doi.org/10.1021/jp104971p

24. Aouani H, Mahboub O, Bonod N et al (2011) Bright unidirectional fluorescence emission of molecules in a nanoaperture with plasmonic corrugations. Nano Lett 11(2):637–644. https://doi.org/10.1021/nl103738d

25. Gordon R (2020) Metal nanoapertures and single emitters. Adv Opt Mater 8(20):2001110. https://doi.org/10.1002/adom.202001110

26. Bethe HA (1944) Theory of diffraction by small holes. Phys Rev 66(7–8):163. https://doi.org/10.1103/PhysRev.66.163

27. Gordon R, Brolo AG, Sinton D et al (2010) Resonant optical transmission through hole-arrays in metal films: physics and applications. Laser Photonics Rev 4(2):311–335. https://doi.org/10.1002/lpor.200810079

28. Thio T, Pellerin KM, Linke RA et al (2001) Enhanced light transmission through a single subwavelength aperture. Opt Lett 26(24):1972–1974. https://doi.org/10.1364/OL.26.001972

29. Ebbesen TW, Lezec HJ, Ghaemi H et al (1998) Extraordinary optical transmission through sub-wavelength hole arrays. Nature 391(6668):667–669. https://doi.org/10.1038/35570

30. Al Balushi AA, Kotnala A, Wheaton S et al (2015) Label-free free-solution nanoaperture optical tweezers for single molecule protein studies. Analyst 140(14):4760–4778. https://doi.org/10.1039/C4AN02213K

31. Verschueren DV, Pud S, Shi X et al (2018) Label-free optical detection of DNA translocations through plasmonic nanopores. ACS Nano 13(1):61–70. https://doi.org/10.1021/acsnano.8b06758

32. Eftekhari F, Escobedo C, Ferreira J et al (2009) Nanoholes as nanochannels: flow-through plasmonic sensing. Anal Chem 81(11):4308–4311. https://doi.org/10.1021/ac900221y

33. Yanik AA, Huang M, Artar A et al (2010) Integrated nanoplasmonic-nanofluidic biosensors with targeted delivery of analytes. Appl Phys Lett 96(2):021101. https://doi.org/10.1063/1.3290633

34. Fan X, White IM (2011) Optofluidic microsystems for chemical and biological analysis. Nat Photonics 5(10):591. https://doi.org/10.1038/nphoton.2011.206

35. Jiang H, Sabarinathan J, Manifar T et al (2009) 3-D FDTD analysis of gold-nanoparticle-based photonic crystal on slab waveguide. J Lightwave Technol 27(13):2264–2270. https://doi.org/10.1109/JLT.2008.2006577

36. Jiang H, Markowski J, Sabarinathan J (2009) Near-infrared optical response of thin film pH-sensitive hydrogel coated on a gold nanocrescent array. Opt Express 17(24):21802–21807. https://doi.org/10.1364/OE.17.021802

37. Jiang H, Sabarinathan J (2010) Effects of coherent interactions on the sensing characteristics of near-infrared gold nanorings. The Journal of Physical Chemistry C 114(36):15243–15250. https://doi.org/10.1021/jp1003598

38. Jiang H, Li T, Yang J et al (2013) Optimization of gold nanoring arrays for biosensing in the fiber-optic communication window. Nanotechnology 24(46):465502. https://doi.org/10.1088/0957-4484/24/46/465502

39. Jiang H, Li T, Ertorer E et al (2013) A biosensor based on periodic arrays of gold nanodisks under normal transmission. Sens Actuators, A 189:474–480. https://doi.org/10.1016/j.sna.2012.08.041

40. Nair RV, Murukeshan VM (2020) (Cu$_2$O-Au) - Graphene - Au layered structures as efficient near infra - red SERS substrates. Sci Rep 10(1):1–10. https://doi.org/10.1038/s41598-020-60874-x

41. Saifur Rahman M, Rikta K, Abdulrazak LF et al (2020) Enhanced performance of SnSe-Graphene hybrid photonic surface plasmon refractive sensor for biosensing applications. Photonics Nanostruct Fundam Appl 39:100779. https://doi.org/10.1016/j.photonics.2020.100779

42. Shabani L, Mohammadi A, Jalali T (2021) Numerical study of plasmonic effects of Ag nanoparticles embedded in the active layer on performance polymer organic solar cells. Plasmonics 17:491–504. https://doi.org/10.1007/s11468-021-01539-x

43. Elrashidi A, Elleithy K (2022) High performance polymer solar cells using grating nanostructure and plasmonic nanoparticles. Polymers 14(5):862. https://doi.org/10.3390/polym14050862

44. Shabani L, Mohammadi A, Jalali T (2022) Performance analysis of polymer bulk heterojunction solar cells with plasmonic nanoparticles embedded into the P3HT:PC$_{61}$BM active layer using the FDTD method. Polymer Bulletin pp 1–22. https://doi.org/10.1007/s00289-022-04521-7

45. Alsayed AE, Ghanim AM, Yahia A et al (2023) Giant localized electromagnetic field of highly doped silicon plasmonic nanoantennas. Sci Rep 13(1):5793. https://doi.org/10.1038/s41598-023-32808-w

46. Ansys Lumerical FDTD Solutions (2023). https://www.lumerical.com/

47. Johnson PB, Christy RW (1972) Optical constants of the noble metals. Phys Rev B 6(12):4370. https://doi.org/10.1103/PhysRevB.6.4370

48. De Abajo FG (2002) Light transmission through a single cylindrical hole in a metallic film. Opt Express 10(25):1475–1484. https://doi.org/10.1364/OE.10.001475

49. Joannopoulos JD, Meade RD, Johnson SG et al (1995) Photonic crystals: molding the flow of light. Princeton University Press, Princeton, NJ, United States

50. Johnson SG, Fan S, Villeneuve PR et al (1999) Guided modes in photonic crystal slabs. Phys Rev B 60(8):5751. https://doi.org/10.1103/PhysRevB.60.5751

51. Escobedo C, Brolo AG, Gordon R et al (2010) Flow-through vs flow-over: analysis of transport and binding in nanohole array plasmonic biosensors. Anal Chem 82(24):10015–10020. https://doi.org/10.1021/ac101654f

52. Prakash S, Pinti M, Bhushan B (2012) Theory, fabrication and applications of microfluidic and nanofluidic biosensors. Philosophical Transactions of the Royal Society A: Mathematical, Physical and Engineering Sciences 370(1967):2269–2303. https://doi.org/10.1098/rsta.2011.0498

53. Wang M, Zhao C, Miao X et al (2015) Plasmofluidics: Merging light and fluids at the micro-/nanoscale. Small 11(35):4423–4444. https://doi.org/10.1002/smll.201500970

54. Escobedo C, Brolo AG, Gordon R et al (2012) Optofluidic concentration: plasmonic nanostructure as concentrator and sensor. Nano Lett 12(3):1592–1596. https://doi.org/10.1021/nl204504s

55. COMSOL Multiphysics (2023). https://www.comsol.com/

56. Tsega EG (2018) Computational fluid dynamics modeling of respiratory airflow in tracheobronchial airways of infant, child, and adult. Comput Math Methods Med 2018:9603451. https://doi.org/10.1155/2018/9603451

57. Hong SC, Kang JS, Lee JE et al (2015) Continuous aerosol size separator using inertial microfluidics and its application to airborne bacteria and viruses. Lab Chip 15(8):1889–1897. https://doi.org/10.1039/C5LC00079C

58. Ohannesian N, Misbah I, Lin SH et al (2020) Plasmonic nanoaperture label-free imaging (PANORAMA). Nat Commun 11(1):5805. https://doi.org/10.1038/s41467-020-19678-w